Batteries

How to cite:
International Edition: doi.org/10.1002/anie.202214126
German Edition: doi.org/10.1002/ange.202214126

Controlling Intermolecular Interaction and Interphase Chemistry Enabled Sustainable Water-tolerance $LiMn_2O_4$||$Li_4Ti_5O_{12}$ Batteries

Qin Li, Chongyin Yang, Jiaxun Zhang, Xiao Ji, Jijian Xu, Xinzi He, Long Chen, Singyuk Hou, Jasim Uddin, Dan Addison, Dalin Sun, Chunsheng Wang,* and Fei Wang**

Abstract: Solid electrolyte interphase (SEI) formation and H_2O activity reduction in Water-in-Salt electrolytes (WiSE) with an enlarged stability window of 3.0 V have provided the feasibility of the high-energy-density aqueous Li-ion batteries. Here, we extend the cathodic potential of WiSE by rationally controlling intermolecular interaction and interphase chemistry with the introduction of trimethyl phosphate (TMP) into WiSE. The TMP not merely limits the H_2O activity via the strong interaction between TMP and H_2O but also contributes to the formation of reinforced SEI involving phosphate and LiF by manipulating the Li^+ solvation structure. Thus, water-tolerance $LiMn_2O_4$ (LMO)||$Li_4Ti_5O_{12}$ (LTO) full cell with a P/N ratio of 1.14 can be assembled and achieve a long cycling life of 1000 times with high coulombic efficiency of >99.9%. This work provides a promising insight into the cost-effective practical manufacture of LMO||LTO cells without rigorous moisture-free requirements.

Introduction

Lithium-ion batteries (LIBs) have been changing our life from portable electronic, electrical vehicles to grid-storage applications. These applications required LIBs to have both high energy and high safety, especially after high-profile fire/explosion incidents.[1–3] The LIBs' safety can be significantly enhanced by replacing the state-of-the-art flammable electrolytes with flame-retarded or even nonflammable electrolytes. Aqueous lithium-ion batteries (ALIBs) are attracting intense attention because of the intrinsic nonflammable nature of the aqueous electrolytes. However, the energy densities of ALIBs are still limited by the narrow stability window of water (<2.0 V).[4–7] Recent advances in the Water-in-Salt electrolyte (WiSE) have significantly expanded the electrochemical window to 3.0 V by the formation of fluorinated solid electrolyte interphase (SEI) from anion reduction, enabling to support some high-energy battery chemistries.[8–11] Obviously, it would be of great importance if the aqueous electrolyte (or its derivatives) can support the commercial cathode/anode couples, and achieve an energy density competitive with the state-of-the-art non-aqueous LIBs.

[*] Q. Li, D. Sun, F. Wang
Department of Materials Science, Fudan University
Shanghai (China)
E-mail: feiw@fudan.edu.cn

C. Yang, J. Zhang, X. Ji, J. Xu, X. He, L. Chen, S. Hou, C. Wang
Department of Chemical and Biomolecular Engineering,
University of Maryland
College Park, MD (USA)
E-mail: chongyinyang@gmail.com
cswang@umd.edu

J. Uddin, D. Addison
Liox Power, Inc.
Pasadena, CA (USA)

In non-aqueous battery chemistries, $LiMn_2O_4$ (LMO)||$Li_4Ti_5O_{12}$ (LTO) cells are safe, environmentally benign, cost-effective, and have a high power density, which is attractive for electric bus applications.[12,13] However, LTO anode suffers from gas evolution in organic electrolytes, resulting in cell degradation. The gas generation is mainly attributed to the parasitic reactions between LTO surface and electrolyte.[14–16] The residual moisture in the electrodes and electrolyte was blamed to be responsible for the gassing because the reduction potential of water of 2.6 V (at pH=7.0) is much higher than the lithiation potential (1.5 V) of LTO.[17–21] And the rigorous moisture-free environment is prerequisite for manufacturing LTO-based batteries. Thus, it is hardly possible to realize the application of LTO in aqueous solutions. However, if the cathodic limit of the WiSE can be reduced to a value below 1.5 V, the gassing problem of LTO in WiSE will be not an issue. But it is very challenging to further widen the electrochemical window to fully operate LTO in the aqueous electrolyte. Although various strategies have shown the expanded cathodic limit through either adding hydrogen bond receptors (such as DMC,[22] DMSO,[23] poly(ethylene glycol) (PEG),[24] sulfolane[25]) in aqueous electrolytes to reduce the free-water, or introducing expensive components like TEAOTF,[26] LiPTFSI,[27] LiBETI[28] to promote the formation of SEI, the full cells, in most cases, could only cycle at a P/N ratio higher than 2.0 to circumvent the effect of hydrogen evolution, even if an additional coating layer is applied to passivate the catalytic surface of LTO. Meanwhile, some added flammable[22,23] or extremely expensive components[28] raised safety and cost concerns of the WiSE, sacrificing the intrinsic advantages of aqueous electrolytes. Therefore, new strategies are needed to develop low-cost and incombustibility-reserving electrolytes with broadened voltage windows to achieve safe batteries with high energy density.

In this work, flame-retardant trimethyl phosphate (TMP) was selected to serve as not only hydrogen bond

acceptors to limit the activity of free water due to its unique water-miscible characteristics and interaction with water molecules, but also as the film-forming additive for robust phosphorus and fluorine rich SEI by manipulating Li^+ solvation structure. They both make for effective kinetic suppression of H_2 evolution on the anode. Therefore, the TMP added here is not a simple substitution for some hydrogen bond receptors. The resultant 9.5 m LiTFSI-TMP-H_2O hybrid electrolytes extended the cathodic limit to 1.2 V (vs Li/Li^+) and enabled the LMO||LTO full cell to be charged/discharged at both a low and a high rate with suppressed gas evolution. Moreover, benefiting from the vital role of TMP in decreasing water activity and reinforcing SEI, the LMO||LTO full cell with limited P/N ratio of 1.14 will get rid of the rigorous moisture-free manufacturing environment. Besides, the potential security concerns can be completely eliminated for the flame-retardant nature of TMP. This approach provides a promising insight to compromise the rigid safety requirement with the aim to minimize the cost of battery manufacture.

Results and Discussion

Molecular Interactions in LiTFSI-TMP-H_2O Hybrid Electrolytes

TMP was selected as the co-solvent here for its fire resistance, low cost, high oxidative stability and water miscibility.[29–32] Saturated TMP-based nonaqueous electrolyte was demonstrated with higher stability than the diluted counterparts.[33,34] To systematically understand the relationship between the property and compositions as well as the intermolecular interactions, a series of LiTFSI-TMP-H_2O hybrid electrolytes was first prepared by mixing the saturated LiTFSI-TMP electrolyte (6.9 m LiTFSI-TMP) with the 21 m LiTFSI-H_2O WiSE at various volume ratios, as listed in Table S1. For convenience, we use molality (m, mol kg^{-1}) to simplify the compositions of hybrid electrolytes. The viscosities of resultant electrolytes varied along with the concentrations. As presented in Figure S1, a higher ratio of TMP dramatically increased the viscosity. The ionic conductivities of hybrid electrolytes with various concentrations were shown in Figure S2a. The conductivity decreases nonlinearly with increasing proportion of TMP. This behavior is due to the combined effects of the viscosity (Figure S1), Li salt concentration and the Li^+ transference number, along with the ion association which leads to the formation of ion pairs and ion aggregates. The 9.5 m LiTFSI-TMP-H_2O electrolyte was then chosen for the subsequent analysis due to its moderate conductivity and viscosity. The Arrhenius plot of this electrolyte was also plotted in Figure S2b and a low activation energy (E_a) of 0.15 eV was fitted out. Despite the addition of the non-aqueous component, the non-flammable nature of the aqueous electrolyte is inherited. As demonstrated in Figure S3, even exposing the electrolyte under a high-temperature propane-oxygen fire, no combustion was observed, thus confirming its high safety.

The liquid structures and the interactions among LiTFSI, TMP, and H_2O in 9.5 m LiTFSI-TMP-H_2O were analyzed using FTIR spectra. Detailed peak deconvolutions in Figure 1a clarified the strong interaction among TMP, LiTFSI and H_2O. For pure water, the analytical spectrum typically consists of five components, relating to the different hydrogen bond engagements and lengths. The peak at the higher wavenumber (3638 cm^{-1}) can be ascribed to the free O–H without hydrogen bonds. Three intermediate components (3222, 3432, 3575 cm^{-1}) are assigned to O–H vibrations engaged in an active local hydrogen-bonded network with surrounding water molecules. The strongest hydrogen bond O–H (solid clusters-like) is responsible for the lowest wavenumber (3043 cm^{-1}). These H_2O molecules with H-bonds account for high mobility compared to the free-OH water.[34–37] Similarly, the multi-peak deconvolution was also utilized for the solvent mixtures. The significant blue shift of the higher wavenumber and disappearance of some peaks attributed to solid clusters-like water (free water) reveal the strong mutual interaction between TMP and H_2O (Figure 1a), indicating the constrained mobility of water molecules in the mixture solvent of TMP and H_2O and the decreased activity of water molecules. Moreover, adding LiTFSI further restricted the water activity due to the synergistic effect of TMP and LiTFSI and lead to the remarkable shift of wavenumber compared to that of WiSE (Figure 1a). The TMP-H_2O intermolecular interactions were also revealed by the down-shift of the band pairs P=O stretch (1277, 1268 cm^{-1})[38–40] (Figure 1b, Figure S4a). The interactions between TMP, LiTFSI and H_2O lower the H_2O activity and construct a solvation structure that differs from pure water or WiSE. As shown in Figure 1c, both ^{17}O NMR signals from TMP (19–75 ppm) and H_2O (0 ppm) are reduced after mixing of the two solvents without LiTFSI, which should be due to the interaction of two solvents with the fracture of hydrogen bonds among water molecules, in agreement with the FTIR spectra.[38,41–43] The interaction was further clarified by changing the molar ratio of the two solvents (TMP: H_2O = 3:1, 1:1, 1:2, 1:3, 0:1) with constant molar ratio of salt/solvent (salt: solvent = 0.378). As displayed in Figure 1d, the ^{17}O signal of H_2O experiences a peak broadening with tiny up-field displacement, which is attributed to the similar shielding effects of TMP as Li^+ to interact with H_2O molecular. The NMR results and the blue shift of O–H stretching in FTIR strongly indicate that the water is further bonded to form a solid-like or ionic-liquid-like state with reduced activity in LiTFSI-TMP-H_2O electrolytes.[44,45] The strong interaction between TMP and H_2O is also confirmed by an incipient increased chemical shift of ^7Li when the TMP/H_2O ratio is lower than 1, as shown in Figure 1e. The subsequent downfield displacement with a higher TMP/H_2O ratio indicates the deshielding effects of the solvation sheath on Li^+. This is because of the higher Gutmann donor number of TMP (23)[46] than that of H_2O (18)[47] and the lower electron density of O in TMP than that in H_2O (Figure S5). Electron density around Li^+ will decrease when TMP is involved in the solvation sheath to replace some H_2O, then the chemical shift of ^7Li NMR towards high values. The corresponding ^7Li NMR spectra of the saturated system (Table S1) studied here are shown in Figure S6. Compared with 21 m WiSE, the chemical shifts

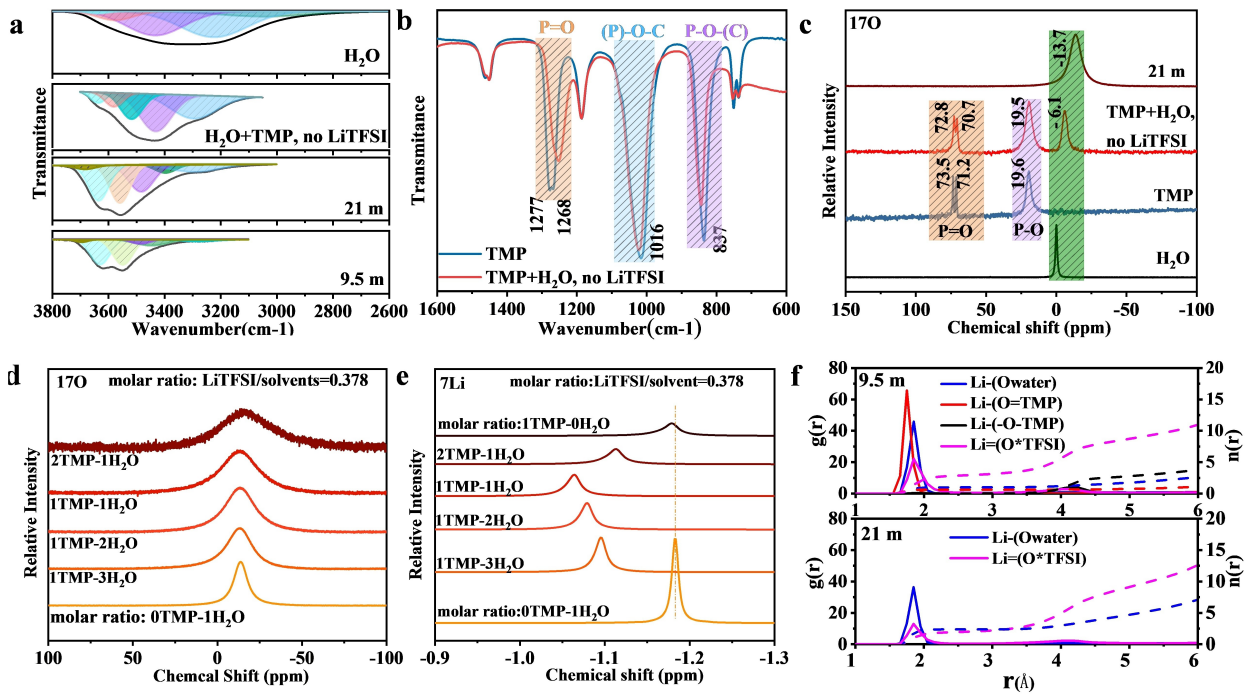

Figure 1. The FTIR spectra of solvents and electrolytes at ranges of a) 2600–3800 cm^{-1} and b) 600–1600 cm^{-1}. c) NMR chemical shifts for ^{17}O nuclei of H_2O and TMP in different solutions. d) Chemical shifts for ^{17}O nuclei of H_2O in different electrolytes. e) Chemical shifts for ^{7}Li nuclei of LiTFSI in different electrolytes. f) The MD simulations of the 9.5 m hybrid electrolyte and 21 m WiSE. Pair distribution function (g(*r*)) and corresponding coordinate number (n(*r*)) for Li^+ in LiTFSI-TMP-H_2O electrolyte and 21 m electrolyte. Ow, O=, –O–, and O* represent the O atom from water, O atom connected with one atom from TMP, O atom connected with two atoms in TMP and O atom in TFSI, respectively.

and full width at half-maximum of ^{7}Li for electrolytes containing TMP changed significantly, also indicating that intermolecular interactions in LiTFSI-TMP-H_2O hybrid electrolytes lead to a solvation structure differing from that of 21 m WiSE.[45]

To further shed light on the solvation structure of 9.5 m LiTFSI-TMP-H_2O electrolyte, classic Molecular dynamics (cMD) simulations were carried out (Figure 1f). In the 9.5 m LiTFSI-TMP-H_2O system, the sharp peak shape of the RDF may result from the strong Coulomb interaction between the Li and O-atoms,[48,49] suggesting that a relatively stable solvation shell was formed around the Li^+.[50–52] Meanwhile, the first pronounced peaks of Ow, O=, –O–, and O* are assigned to the coordination between Li and O from water, one atom from TMP, two atoms from TMP and O from $TFSI^-$, respectively, also indicating that $TFSI^-$, H_2O, and TMP are all participating in the Li^+ cation coordination. In addition, it was shown that the water molecule in the solvation structure decreased from 2.36 in 21 m WiSE to 1.02 in 9.5 m LiTFSI-TMP-H_2O electrolyte per Li^+ solvation shell, while the fraction of $TFSI^-$ increased from 1.96 in 21 m WiSE to 2.85 in 9.5 m LiTFSI-TMP-H_2O electrolyte per Li^+ solvation shell. The $TFSI^-$- and TMP-involved solvation structure was supposed to form a reinforced SEI layer containing LiF and phosphate, owing to the decomposition of $TFSI^-$ and the reduction of TMP, which may further contribute to enhanced redox stability of electrolyte.

Reinforced Interphase Chemistry in LiTFSI-TMP-H_2O Hybrid Electrolytes

To evaluate SEI formation progress and verify the reinforced SEI chemistry, cyclic voltammetry (CV), linear sweep voltammetry (LSV), X-ray photoelectron spectroscopy (XPS) and Cryo-TEM were carried out. First, a detailed cathodic CV was performed with 9.5 m LiTFSI-TMP-H_2O electrolyte by a three-electrode system with Ag/AgCl electrode as the reference electrode (Figure S7). As expected, the gradual degradation of reduction current with cycling evidences the stepwise formation of the SEI ascribed to the possible concurrent decomposition of TMP and LiTFSI.[53,54] Accordingly, the cathodic limiting potential is considered to be 1.2 V vs Li/Li^+. Then the LSV results (Figure 2a) of four electrolytes showed that the electrochemical stable window extends to 3.7 V when the TMP-based portion is higher than 50 % vol with an anodic limiting potential of about 4.9 V vs. Li/Li^+, which is benefited from the decreased water activity and SEI formation. The broadened electrochemical stable window, much wider than the 3.0 V of 21 m WiSE, could theoretically support $Li_4Ti_5O_{12}$ (LTO) anode and $LiMn_2O_4$ (LMO) cathode for high-energy aqueous LIBs. As shown in the CV results of LTO and LMO electrode with 9.5 m LiTFSI-TMP-H_2O electrolyte in a three-electrode cell (Figure 2a), a pair of characteristic reversible redox peaks emerged around 1.6/1.9 V vs Li/Li^+ corresponding to the lithiation/delithiation reaction of LTO instead of hydrogen evolution. Broad peaks

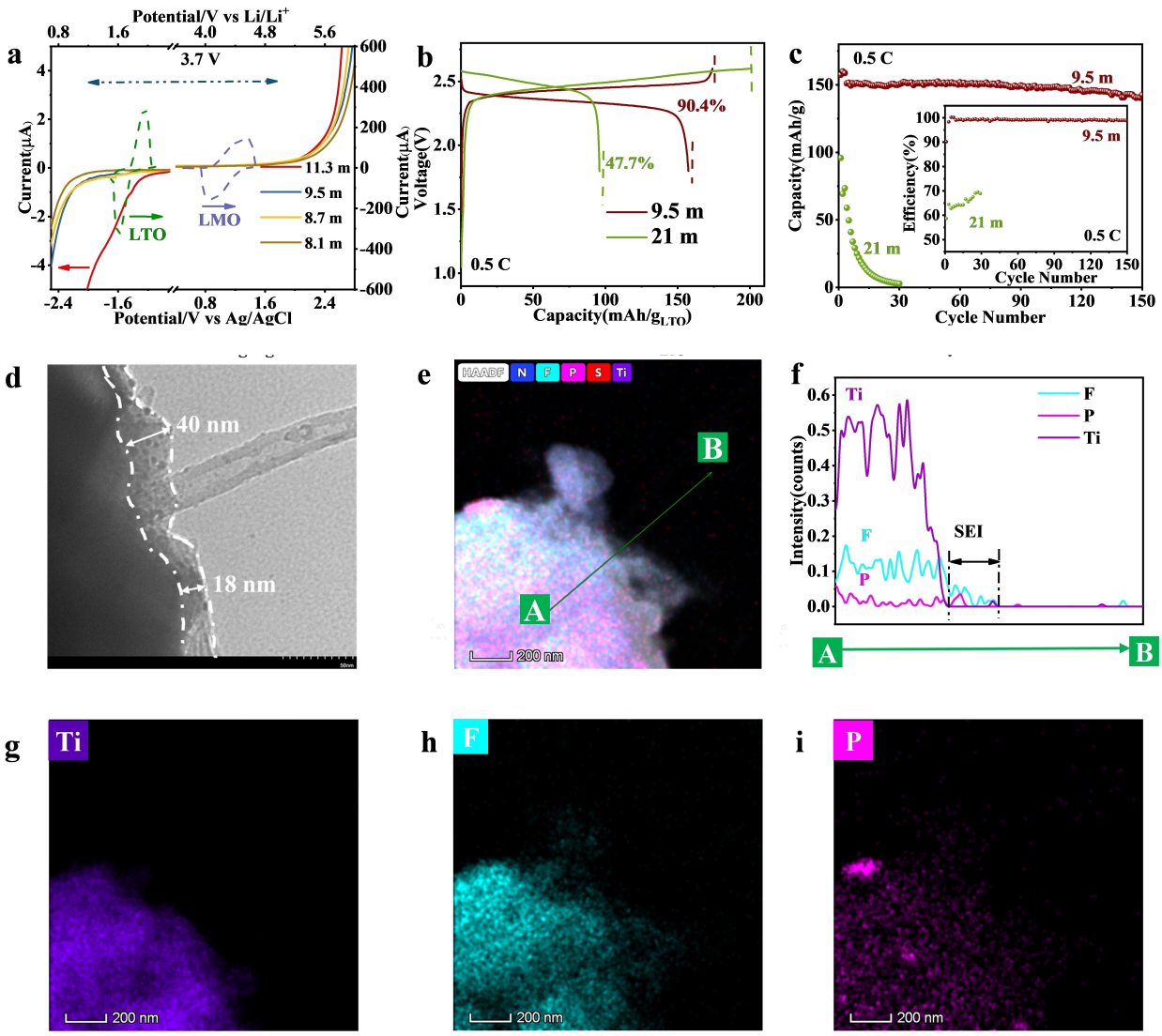

Figure 2. a) The electrochemical stability window of hybrid electrolytes. Measurements were taken at different concentrations with LSV on the aluminum electrode (voltage range between −0.2 V and −2.6 V) and titanium electrode (voltage range between 0.2 V and 3.0 V vs Ag/AgCl) at 10 mV s^{-1}, wherein the potential has been converted to Li/Li^+ reference for convenience. The cyclic voltammetry (CV) of active electrodes (LTO and LMO) was collected at 0.5 mV s^{-1} in 9.5 m LiTFSI-TMP-H_2O electrolyte. b) The voltage profiles and c) cycling performance of LTO anode in 9.5 m LiTFSI-TMP-H_2O electrolyte and 21 m WiSE at 0.5 C. The capacity ratio of LMO to LTO was set as 5 : 1. The capacity presented here was based on LTO anode. d) Cryo-TEM image of LTO after cycling in 9.5 m LiTFSI-TMP-H_2O electrolyte. e) Overlapped HAADF image and f) EDS line scan of Ti, P and F signals. The corresponding EDS maps of g) Ti, h) F and i) P elemental distribution.

located at approximately 4.0 and 4.5 V vs Li/Li^+ can be observed for redox reactions of the LMO cathode. Thus, the electrochemical couple of LTO and LMO, totally enveloped inside the electrochemical stability window of the LiTFSI-TMP-H_2O hybrid electrolytes, was chosen for subsequent demonstration of the generated SEI and evaluation of electrochemical performance.

The morphology and structure of LTO and LMO powder before cycling were characterized using XRD, SEM and TEM. As shown in Figure S8a, LTO exhibited a typical spinel structure with the space group *Fd3m* (JCPDS No. 49-0207). The micro-sized LTO secondary sphere particles consisted of primary nanoparticles with a size of 500 nm (Figure S8b–d). From the HRTEM in Figure S8e-f, lattice fringes of 0.48 nm corresponding to the (111) crystalline planes of LTO were observed. The crystalline structure of LMO was also identified as a cubic spinel structure (JCPDS No. 35-0782) with the *Fd3m* space group, as shown in Figure S9a. The SEM images (Figure S9b–c) show that the LMO particles have a truncated octahedral morphology with a size range of 1–10 μm.

Cycling performances of the LTO anode and relevant post-analysis were conducted in half-cells with LMO||LTO two-electrode system. To minimize the interference of the cathode with limited lithium source, much excess LMO is preferred when applied as the counter electrode. Thus, a

high P/N capacity ratio of 5.0 is selected. Since LMO shows high efficiency in 9.5 m LiTFSI-TMP-H_2O hybrid electrolyte (Figure S10), the coulombic efficiency (CE) of the LMO||LTO cell was determined by the LTO. The electrochemical behaviors of LMO||LTO cells at 2 C in electrolytes with various concentrations were compared in Figure S11. All cells display similar electrochemical behaviors, such as an obvious plateau at around 2.4 V. However, differences exist in the polarization, capacity and coulombic efficiency of cells cycled in different electrolytes due to the diverse ionic conductivity, viscosity and electrochemical stability. As shown in Figure S11, LMO||LTO cell with 11.3 m LiTFSI-TMP-H_2O exhibits the highest initial capacity of 134.9 mAh g^{-1} due to the lowest viscosity and highest conductivity of the electrolyte, but the CE is the lowest because of the worst reduction stability, resulting in a faster capacity decay. The efficiency and cycle stability improved when the electrolyte concentration is below 9.5 m whose reduction potential is extended to 1.2 V. Nevertheless, the discharge capacity decreased to 95 mAh g^{-1} when the electrolyte concentration decreased to 8.1 m, due to its highest viscosity and lowest conductivity. By comparison, the 9.5 m electrolyte possesses a relatively high ionic conductivity (1.0 mS cm^{-1}), a low viscosity (150 cP), and a wide electrochemical window (3.7 V). And the cells cycled in 9.5 m LiTFSI-TMP-H_2O electrolyte exhibited the best electrochemical performance (high capacity, high CE and good cycling stability). Thus, we applied this electrolyte as the focus for the subsequent experiments due to its best overall properties. As presented in Figure 2b, the initial CE of LTO anode at 0.5 C in the 9.5 m LiTFSI-TMP-H_2O electrolyte is about 90.4 %, much higher than that of 21 m WiSE (58.7 %), indicating a significantly lower degree of H_2O decomposition. As a result, good compatibility of 9.5 m electrolyte with the LTO electrode was evidenced by a stable charge/discharge cycling for 150 cycles with an average capacity decay rate of 0.063 % per cycle at a low rate of 0.5 C (Figure 2c, Figure S12a). In sharp comparison, the cell using 21 m WiSE kept decaying and no capacity was delivered after only 30 cycles (Figure 2c, Figure S12b). This can be attributed to the efficient kinetic suppression of H_2 evolution resulting from the decreased water activity and generated robust SEI.

To confirm the effective barrier of the SEI formed on the cycled LTO electrode, XPS and Cryo-TEM were conducted. The morphology and composition of the SEI layer formed on LTO anode in 9.5 m electrolyte were first characterized under the assistance of Cryo-TEM. The magnified view in Figure 2d clearly revealed a mosaic SEI and the thickness of this outermost layer ranges from ≈18 to ≈40 nm. Meanwhile, the overlapped HAADF image in Figure 2e reveals the coexistence of the inorganic F- and P-containing compounds in the SEI, suggesting that the TMP and $TFSI^-$ are together involved in robust SEI formation. The corresponding EDS line scanning from A to B indicates the gradient distribution of F and P elements across the interface (Figure 2f), which further clearly confirmed the multilayer-mosaic characteristic inside the SEI formed in 9.5 m electrolyte. Moreover, the element mappings in Figure 2g–i clearly demonstrated a relatively uniform spatial distribution of Ti, F and P elements upon the LTO interface.

To reconfirm the fluorine-rich and phosphatic characteristics of the SEI layer, XPS depth analysis was further conducted on the formed SEI layer in 9.5 m electrolyte. For comparison, the SEI layer on LTO electrode in 21 m electrolyte was also characterized. The evolution of the chemical composition against etching time was shown in Figure S13. The most significant distinction of LTO electrodes cycled in these two electrolytes lies in the existence of P, deriving from the decomposition by-products of TMP solvent, which takes up ≈0.72 at% before etching and still maintains with 120 s etching in 9.5 m LiTFSI-TMP-H_2O electrolyte. In the meantime, a lower F, S and N content (17.8 at%, 0.77 at% and 1.34 at%, respectively) resulting from $TFSI^-$ was seen upon TMP addition (9.5 m LiTFSI-TMP-H_2O) indicates that regulated solvation structure has dramatically alleviated the unfavorable decomposition of electrolytes. In addition, the content of F element in 9.5 m LiTFSI-TMP-H_2O exhibits a relatively slow decrease upon etching than that recorded for the 21 m electrolyte. These differences in composition and content suggest that the SEI formed in 9.5 m electrolyte containing phosphate and F-containing compounds is dense and robust. Furthermore, the deconvoluted core spectra of C 1s, O 1s, F 1s, Ti 2p, and P 2p are presented in Figure 3. As for the C 1s spectra in Figure 3a, the main peaks at 284.8, 285.4, 286.9, 290.1, 291.9 eV and 294.2 eV are assigned to C–C, C–H, C–O, C=O, CO_3^{2-} and C–F_3, respectively. As the etching depth proceeds on, signals of C–O, C=O, CO_3^{2-} and C–F_3 gradually fade and even vanish, indicating decreased organic species approaching the LTO surface. These can also be confirmed by the changes of C–O/O–H peaks in O 1s spectra (Figure 3b) and C–F_3 peaks in F 1s spectra (Figure 3c). In comparison, for the XPS spectra collected from LTO cycled in 21 m electrolyte (Figure S14), these organic species (C–O, C=O, CO_3^{2-} and C–F_3 in C 1s spectra, C–O/O–H in O 1s spectra) are much stronger than that observed in 9.5 m electrolyte, revealing the accumulation of organic-rich SEI layer. The F 1s (Figure 3c) detected therein around 686.0 eV is identified to be LiF due to the reduction of LiTFSI. Some residual LiTFSI on the electrode surface accounts for the C–F_3 at 690.1 eV, and the peak at 689.1 eV comes from PVDF binder in the electrode.[8,9,22,23] The increased intensity of the LiF species (Figure 3c) with etching depth indicates LiF-riched inner SEI. As for the F 1s obtained in 21 m electrolyte, a similar trend that signals of LiF increase with etching can be observed, and LiF remains dominant in the inner layer. However, this LiF layer accompanied by porous organic species cannot shield the LTO anode against the attack by continuous decomposition of H_2O in 21 m electrolyte. In addition, the P 2p spectra (Figure 3e), corresponding to Li_3PO_4 or phosphate species, resulted from the decomposition of TMP[55,56] and demonstrated the contribution of TMP to the inorganic components of SEI on LTO surface cycled in the 9.5 m LiTFSI-TMP-H_2O electrolyte. The existence of Li_3PO_4 and phosphate species is further revealed by the peaks at 532.6 eV and 534.6 eV in O 1s peaks in Figure 3b. In

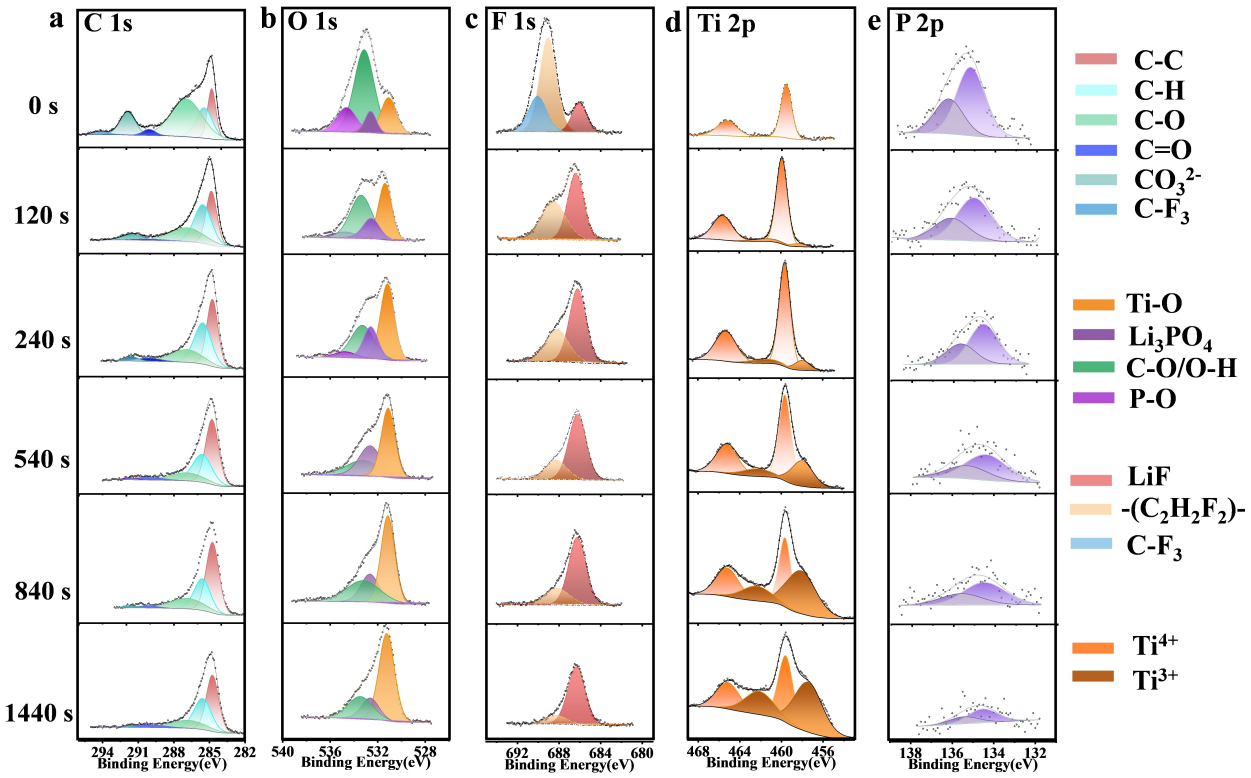

Figure 3. XPS spectra with depth analysis of LTO electrodes after cycling in 9.5 m electrolyte at 0.5 C. a) C 1s, b) O 1s, c) F 1s, d) Ti 2p and e) P 2p.

summary, the above XPS results with different etching times strongly suggest that the presence of TMP in the 9.5 m electrolyte promotes the generation of a stable, robust SEI layer with phosphate and LiF species. The correlation of the SEI layer and electrochemical performance of LTO electrodes strongly suggested that the reinforced LiF-Li_3PO_4 SEI can effectively suppress hydrogen evolution.

As for the LMO cathode cycled in 9.5 m electrolyte, XRD, SEM, TEM and XPS characterization were conducted to reveal the variations of morphology and structure. As shown in Figure S15, there is no significant shifting and lowering of the diffraction peaks of LMO phases due to structural decay, indicating no new bulk phase formation and the structural stability of LMO after cycling in 9.5 m LiTFSI-TMP-H_2O electrolyte. The SEM images (Figure S16a, b) show that the LMO particles before and after cycling exhibit no differences in the surface morphology and all have a truncated octahedral morphology. The structure variation of the LMO before and after cycling was further characterized by TEM. The well-defined crystal bulk structure with a *d*-spacing of 0.48 nm was well preserved. In addition, both samples showed a smooth surface and no distinct amorphous layer was formed on the cycled LMO surface (Figure S16c, d), indicating no significant decomposition of electrolytes on the LMO.

XPS measurement with Ar^+ etching was further conducted to characterize the cycled LMO interface. The atomic percentage of the chemical composition on cycled LMO as a function of etching time is presented in Figure S17. The few amounts of P elements suggest the absence of TMP decomposition. The high contents of O and C elements and low F percentage indicate an organic surface on LMO, which may be derived from the residual electrolyte components. Detailed resolutions of C 1s, O 1s, F 1s and P 2p XPS spectra were displayed in Figure S18. Different from the SEI formed on the cycled LTO anode, the fluorine-containing species from the salt decomposition as well as the phosphate from the TMP solvents were not detected on the cycled LMO surface, indicating no CEI layer come from electrolyte decomposition, in line with the TEM results. The trace amount of as-formed organic species observed in C 1s and O 1s spectra may result from residual electrolytes, which can be confirmed by their rapidly decreased intensity upon etching. These fluorine-containing species deposited on the cathode surface even after prolonged sputtering may result from the $-(CF)_n-$ species during etching.

In summary, the morphology and structure of the LMO cathode are well maintained after cycling in 9.5 m electrolyte, and no distinct CEI layer derived from electrolyte decomposition was observed on the surface.

LMO||LTO Full Cells at P/N Capacity of 1.14 in 9.5 m LiTFSI-TMP-H_2O Hybrid Electrolyte

Benefited from the protective passivation layer formed in the 9.5 m LiTFSI-TMP-H_2O electrolyte, a practical P/N capacity ratio of 1.14 was selected to assemble LMO||LTO full cells to evaluate the comprehensive electrochemical performance at the practical cell level. The limited cathode

capacity excess was designed to compensate for the irreversible loss at the initial SEI formation process and to maximize cell-level specific energy. Typical charge/discharge curves at various cycles between 1.8 V and 2.8 V are displayed in Figure 4a. The initial discharge capacity is about 124 mAh g^{-1} (calculated based on the mass of the anode) at 2 C with a voltage plateau at 2.4–2.6 V, corresponding to an initial efficiency of 90 %. SEI formation along with a certain extent of H_2O decomposition results in this irreversible capacity loss. Stable cycling was observed after the gradual passivation process (Figure 4b), which can be concluded from the gradual increasing resistance in the EIS spectra of various cycles (Figure S19). The capacity retention of 72 % relative to the initial capacity can be obtained after 200 cycles at 2 C with a stable CE approaching 100 % (Figure 4b). However, the performance of full cell cycled in control 21 m WiSE experienced a rather severe capacity decay due to remarkable H_2O decomposition. Almost no capacity was retained after 30 cycles, further evidencing the feasibility of the TMP/H_2O-based electrolyte and a long-term stabilization effect for the cycling of LIBs by the addition of TMP.

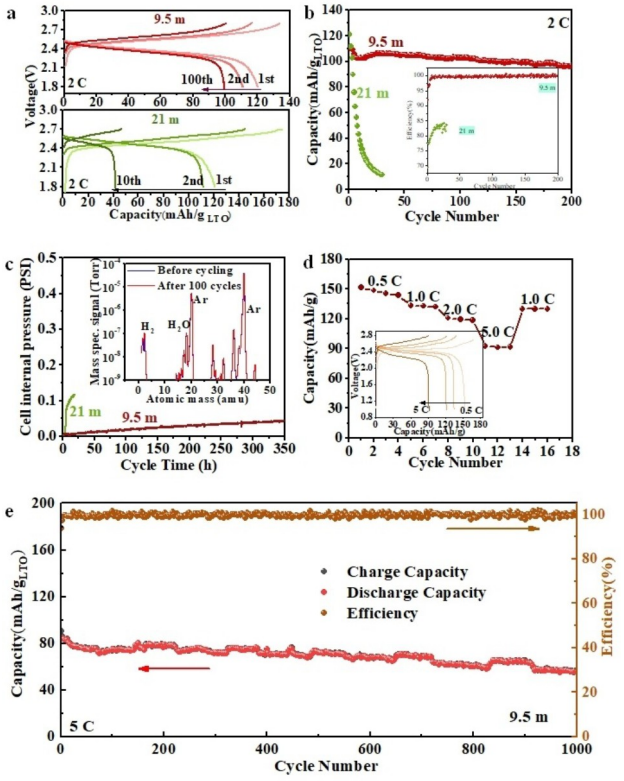

Figure 4. a) Typical voltage profiles of LMO||LTO full cells in 9.5 m LiTFSI-TMP-H_2O electrolyte and 21 m WiSE at a constant current of 2 C (capacity based on LTO). b) The corresponding cycling stability of LMO||LTO full cells in different electrolytes at 2 C. c) In situ monitoring of internal gas pressure for LMO||LTO cells with various electrolytes during long cycling. Inset: gas compositions of LMO||LTO cell with 9.5 m electrolyte before and after 100 cycles examined by mass spectra. d) The rate performance of LMO||LTO cells. Inset: the corresponding charge/discharge voltage profiles of the LMO||LTO full cell at various rates. e) Cycling stability of LMO||LTO full cells at a constant current of 5 C.

To further reconfirm the superiority of the robust SEI and the restrictive water activity with the assistance of TMP, the self-discharge of a fully charged full cell was evaluated by monitoring the variation of the potential over time. The cycling protocol was set as follows: the full cells were first cycled 10 times at 0.5 C, then charged to 100 % SOC and rested for different times. The decay of open circuit voltage (OCV) during rest at 100 % SOC was monitored as shown in Figure S20a. After the resting period, potential change can be observed in both 21 m and 9.5 m electrolytes, indicating the existence of parasitic reactions at the LTO anode. In stark contrast, the voltage of LMO||LTO cell with 21 m electrolyte fades rapidly from 2.75 V to ≈1.4 V within 24 h, whereas the voltage of LMO||LTO cell with 9.5 m electrolyte reduces from 2.74 V to ≈2.6/2.6/2.58 V after resting 12 h, 24 h, 36 h, respectively. Meanwhile, the corresponding discharge capacity obtained after 24 h resting is reported in Figure S20b. No capacity was retained in 21 m electrolyte whereas capacity retention of 71.7 % was observed in 9.5 m electrolyte, suggesting the improved storage capability. The suppression of this self-discharge phenomenon can be attributed to the superior protection of robust SEI as well as the strengthened intrinsic stability of 9.5 m electrolyte over those in 21 m electrolyte.

In situ pressure measurement was applied to monitor the gas evolution in LMO||LTO cells during cycling in different electrolytes to further verify the effective barrier of SEI layer and decreased water activity. As shown in Figure 4c and Figure S21, the cell pressure increased rapidly in 21 m WiSE due to the serious water decomposition, which accounted for the poor cycling stability. After only 10 h, the cell pressure approached 0.1 PSI (0.0068 atm). The cells cycled in 11.3 m and 13.6 m electrolytes also exhibited a relative fast-growing pressure due to the H_2O decomposition, which is consistent with their electrochemical window (2.0–4.9 V, Figure 2a) and the efficiency of LMO||LTO cells (CE < 98 %, Figure S11). These may be due to inadequate passivation of uneven and thicker SEI. In contrast, only a slight pressure increase was recorded for the cell using 9.5 m, 8.7 m and 8.1 m LiTFSI-TMP-H_2O electrolyte. The cell pressure with 9.5 m LiTFSI-TMP-H_2O electrolyte after 300 h only increased by 0.044 PSI (ΔP = 0.00299 atm), corresponding to about 1.1×10^{-5} mol gas produced. The generated gas was further analyzed by the mass spectrum, as shown in the inset in Figure 4c. A very small amount of H_2 was generated during 100 cycles, which is about 7.622×10^{-8} mol mAh^{-1}. Supposing the production of hydrogen is the only side reaction in the battery, then the electrons consumed for H_2 generation is about 3.811×10^{-8} mol mAh^{-1} (3.67×10^{-3} C/3.6 C), corresponding to an average CE of 99.9 % measured during electrochemical cycling. The suppressed water decomposition is attributed to the effective passivation with robust SEI on the LTO anode and decreased water activity. In addition, the resultant reinforced SEI with LiF-Li_3PO_4 species can maintain the structural stability of LTO during lithiation/delithiation by restraining H_2 evolution, as confirmed by the XRD analysis

(Figure S22) of LTO electrode before and after cycling in different electrolytes. The XRD peaks of LTO cycled in 9.5 m LiTFSI-TMP-H_2O electrolyte are almost the same as that of LTO before cycling. However, upward-shifting and peak broadening were observed from the XRD of LTO cycled in 21 m WiSE, indicating structural failure due to severe H_2 evolution or proton co-intercalation.

The rate capability of the LMO||LTO full cell was shown in Figure 4d, a discharge capacity of 152 mAh g^{-1} at the low rate of 0.5 C can be obtained. After cycling at the high rate of 5 C, the capacity could fully recover when the rate returned. Ultra-long cycling test at 5 C (Figure 4e) shows a low capacity decay rate of 0.034 % per cycle for 1000 cycles. During the cycling, the CE kept above 99.9 %. It is worth mentioning that consumption of the limited cathode Li source will also lead to capacity decay and an increase in polarization of the full cell. The fluctuations during cycling at 5 C were attributed to the fluctuant temperature, which was more sensitive at a high rate. In all, stable cycling of LMO||LTO full cells with limited capacity excess were successfully achieved due to reinforced interphase chemistry and intermolecular interaction in TMP/H_2O-based electrolyte.

Conclusion

In summary, we demonstrated for the first time that the LMO||LTO full cell with limited capacity excess can steadily cycle at a low rate in the presence of water by applying the self-extinguishing LiTFSI-TMP-H_2O hybrid electrolyte. The interaction between TMP and H_2O decreased the water activity. The synergistic decomposition of TMP and LiTFSI reinforced the SEI generated on the LTO surface. These two superiorities contributed to the extended electrochemical stable window to 3.7 V with suppressed gas evolution on the LTO electrode. The LMO||LTO full cell with a P/N capacity ratio of 1.14 assembled in open-air can deliver long-term stable cycling at 5 C in 9.5 m LiTFSI-TMP-H_2O hybrid electrolyte, corresponding to a low capacity decay rate of 0.034 % per cycle for 1000 cycles, indicating the unique moisture-tolerance characteristic of LMO||LTO cells in LiTFSI-TMP-H_2O electrolyte. It is worth noting that cost can be markedly reduced by the decreased LiTFSI concentration and decreased requirements for the manufacturing environment. In addition, the safety performance can be markedly improved with the presence of the non-flammable TMP. The success of this work will provide a novel and sustainable strategy for developing water-tolerance LIBs and promote their penetration into the electric devices market.

Conflict of Interest

The authors declare no conflict of interest.

Data Availability Statement

The data that support the findings of this study are available on request from the corresponding author. The data are not publicly available due to privacy or ethical restrictions.

Keywords: Intermolecular Interaction · Interphase Chemistry · Water-tolerance Characteristics · LMO||LTO Batteries

[1] K. Xu, *Chem. Rev.* **2004**, *104*, 4303.
[2] Y. Miao, P. Hynan, A. Jouanne, A. Yokochi, *Energies* **2019**, *12*, 1074.
[3] X. Zhu, F. Meng, Q. Zhang, L. Xue, H. Zhu, S. Lan, Q. Liu, J. Zhao, Y. Zhuang, Q. Guo, B. Liu, L. Gu, X. Lu, Y. Ren, H. Xia, *Nat. Sustainability* **2021**, *4*, 392.
[4] Z. Chang, Y. Yang, M. Li, X. Wang, Y. Wu, *J. Mater. Chem. A* **2014**, *2*, 10739.
[5] A. Eftekhari, *Adv. Energy Mater.* **2018**, *8*, 1801156.
[6] W. Li, J. R. Dahn, D. S. Wainwright, *Science* **1994**, *264*, 1115.
[7] W. Li, J. R. Dahn, *J. Electrochem. Soc.* **1995**, *142*, 1742.
[8] L. Suo, O. Borodin, T. Gao, M. Olguin, J. Ho, X. Fan, C. Luo, C. Wang, K. Xu, *Science* **2015**, *350*, 938.
[9] L. Suo, O. Borodin, W. Sun, X. Fan, C. Yang, F. Wang, T. Gao, Z. Ma, M. Schroeder, A. Cresce, S. M. Russell, M. Armand, A. Angell, K. Xu, C. Wang, *Angew. Chem. Int. Ed.* **2016**, *55*, 7136; *Angew. Chem.* **2016**, *128*, 7252.
[10] Y. Yokoyama, T. Fukutsuka, K. Miyazaki, T. Abe, *J. Electrochem. Soc.* **2018**, *165*, A3299.
[11] X. Yuan, F. Ma, L. Zuo, J. Wang, N. Yu, Y. Chen, Y. Zhu, Q. Huang, R. Holze, Y. Wu, T. Ree, *Electrochem. Energy Rev.* **2021**, *4*, 1.
[12] M. M. Thackeray, W. I. F. David, P. G. Bruce, J. B. Goodenough, *Mater. Res. Bull.* **1983**, *18*, 461.
[13] L. Aldon, P. Kubiak, M. Womes, J. C. Jumas, J. Olivier-Fourcade, J. L. Tirado, J. I. Corredor, C. Perez Vicente, *Chem. Mater.* **2004**, *16*, 5721.
[14] Y. He, B. Li, M. Liu, C. Zhang, W. Lv, C. Yang, J. Li, H. Du, B. Zhang, Q. Yang, J. Kim, F. Kang, *Sci. Rep.* **2012**, *2*, 913.
[15] B. Li, C. Han, Y. He, C. Yang, H. Du, Q. Yang, F. Kang, *Energy Environ. Sci.* **2012**, *5*, 9595.
[16] C. Wang, S. Wang, Y. He, L. Tang, C. Han, C. Yang, M. Wagemaker, B. Li, Q. Yang, J. Kim, F. Kang, *Chem. Mater.* **2015**, *27*, 5647.
[17] W. Lv, J. Gu, Y. Niu, K. Wen, W. He, *J. Electrochem. Soc.* **2017**, *164*, A2213.
[18] I. Belharouak, G. M. Koenig, Jr., T. Tan, H. Yumoto, N. Ota, K. Amine, *J. Electrochem. Soc.* **2012**, *159*, A1165.
[19] M. He, E. Castel, A. Laumann, G. Nuspl, P. Novák, E. J. Berg, *J. Electrochem. Soc.* **2015**, *162*, A870.
[20] R. Bernhard, S. Meini, H. A. Gasteiger, *J. Electrochem. Soc.* **2014**, *161*, A497.
[21] Q. Wang, J. Zhang, W. Liu, X. Xie, B. Xia, *J. Power Sources* **2017**, *343*, 564.
[22] F. Wang, O. Borodin, M. S. Ding, M. Gobet, J. Vatamanu, X. Fan, T. Gao, N. Eidson, Y. Liang, W. Sun, S. Greenbaum, K. Xu, C. Wang, *Joule* **2018**, *2*, 927.
[23] Q. Nian, J. Wang, S. Liu, T. Sun, S. Zheng, Y. Zhang, Z. Tao, J. Chen, *Angew. Chem. Int. Ed.* **2019**, *58*, 16994; *Angew. Chem.* **2019**, *131*, 17150.
[24] J. Xie, Z. Liang, Y. Lu, *Nat. Mater.* **2020**, *19*, 1006.
[25] Y. Wang, T. Wang, D. Dong, J. Xie, Y. Guan, Y. Huang, J. Fan, Y. Lu, *Matter* **2022**, *5*, 162.
[26] L. Jiang, L. Liu, J. Yue, Q. Zhang, A. Zhou, O. Borodin, L. Suo, H. Li, L. Chen, K. Xu, Y. Hu, *Adv. Mater.* **2020**, *32*, 1904427.

[27] S. Ko, Y. Yamada, K. Miyazaki, T. Shimada, E. Watanabe, Y. Tateyama, T. Kamiya, T. Honda, J. Akikusa, A. Yamada, *Electrochem. Commun.* **2019**, *104*, 106488.
[28] Y. Yamada, K. Usui, K. Sodeyama, S. Ko, Y. Tateyama, A. Yamada, *Nat. Energy* **2016**, *1*, 16129.
[29] X. Wang, E. Yasukawa, S. Kasuya, *J. Electrochem. Soc.* **2001**, *148*, A1058.
[30] K. Xu, S. Zhang, J. L. Allen, T. R. Jow, *J. Electrochem. Soc.* **2003**, *150*, A161.
[31] K. Matsumoto, K. Nakahara, K. Inoue, S. Iwasa, K. Nakano, S. Kaneko, H. Ishikawa, K. Utsugi, R. Yuge, *J. Electrochem. Soc.* **2014**, *161*, A831.
[32] K. Sankaran, V. Vidya, K. S. Viswanathan, L. George, S. Singh, *J. Phys. Chem. A* **1998**, *102*, 2944.
[33] X. Wang, C. Yamada, H. Naito, G. Segami, K. Kibe, *J. Electrochem. Soc.* **2006**, *153*, A135.
[34] J. Wang, Y. Yamada, K. Sodeyama, E. Watanabe, K. Takada, Y. Tateyama, A. Yamada, *Nat. Energy* **2018**, *3*, 22.
[35] B. Auer, R. Kumar, J. R. Schmidt, J. L. Skinner, *Proc. Natl. Acad. Sci. USA* **2007**, *104*, 14215.
[36] Y. Chen, Y. Zhang, L. Zhao, *Phys. Chem. Chem. Phys.* **2004**, *6*, 537.
[37] C. de Lozé, M. H. Baron, *Chem. Phys. Lett.* **1971**, *9*, 103.
[38] S. Tsubouchi, S. Suzuki, K. Nishimura, T. Okumura, T. Abe, *J. Electrochem. Soc.* **2018**, *165*, A680.
[39] W. Yan, L. Yan, J. Duan, C. Jing, *J. Hazard. Mater.* **2014**, *273*, 53.
[40] J. H. Clark, M. Green, R. G. Madden, *Chem. Commun.* **1983**, 136.
[41] S. K. McIntyre, T. M. Alam, *Magn. Reson. Chem.* **2007**, *45*, 1022.
[42] X. Bogle, R. Vazquez, S. Greenbaum, A. Wald Cresce, K. Xu, *J. Phys. Chem. Lett.* **2013**, *4*, 1664.
[43] J. A. Gerlt, P. C. Demou, S. Mehdi, *J. Am. Chem. Soc.* **1982**, *104*, 2848.
[44] M. R. Lukatskaya, J. I. Feldblyum, D. G. Mackanic, F. Lissel, D. L. Michels, C. Yi, Z. Bao, *Energy Environ. Sci.* **2018**, *11*, 2876.
[45] M. Takamoto, T. Ueda, S. Himeno, *J. Electroanal. Chem.* **2002**, *521*, 132.
[46] Y. Marcus, *J. Solution Chem.* **1984**, *13*, 599.
[47] L. Cao, D. Li, E. Hu, J. Xu, T. Deng, L. Ma, Y. Wang, X. Yang, C. Wang, *J. Am. Chem. Soc.* **2020**, *142*, 21404.
[48] R. Takagi, F. Hutchinson, P. A. Madden, A. K. Adya, M. Gaune-Escard, *J. Phys. Condens. Matter* **1999**, *11*, 645.
[49] H. S. Dhattarwal, H. K. Kashyap, *J. Phys. Chem. B* **2022**, *126*, 5291.
[50] H. Zhang, F. Chen, O. Lakuntza, U. Oteo, L. Qiao, M. Martinez-Ibañez, H. Zhu, J. Carrasco, M. Forsyth, M. Armand, *Angew. Chem. Int. Ed.* **2019**, *58*, 12070; *Angew. Chem.* **2019**, *131*, 12198.
[51] D. E. Galvez-Aranda, J. M. Seminario, *J. Electrochem. Soc.* **2021**, *168*, 040511.
[52] A. von Wald Cresce, M. Gobet, O. Borodin, J. Peng, S. M. Russell, E. Wikner, A. Fu, L. Hu, H. Lee, Z. Zhang, X. Yang, S. Greenbaum, K. Amine, K. Xu, *J. Phys. Chem. C* **2015**, *119*, 27255.
[53] N. Yoshimoto, Y. Niida, M. Egashira, M. Morita, *J. Power Sources* **2006**, *163*, 238.
[54] S. F. Lux, L. Terborg, O. Hachmöller, T. Placke, H.-W. Meyer, S. Passerini, M. Winter, S. Nowak, *J. Electrochem. Soc.* **2013**, *160*, A1694.
[55] A. C. Kozen, A. J. Pearse, C. Lin, M. Noked, G. W. Rubloff, *Chem. Mater.* **2015**, *27*, 5324.
[56] M. S. Milien, U. Tottempudi, M. Son, M. Ue, B. L. Lucht, *J. Electrochem. Soc.* **2016**, *163*, A1369.

Manuscript received: September 24, 2022
Accepted manuscript online: October 5, 2022
Version of record online: ■■, ■■

Research Articles

Batteries

Q. Li, C. Yang,* J. Zhang, X. Ji, J. Xu, X. He, L. Chen, S. Hou, J. Uddin, D. Addison, D. Sun, C. Wang,* F. Wang* . **e202214126**

Controlling Intermolecular Interaction and Interphase Chemistry Enabled Sustainable Water-tolerance $LiMn_2O_4||Li_4Ti_5O_{12}$ Batteries

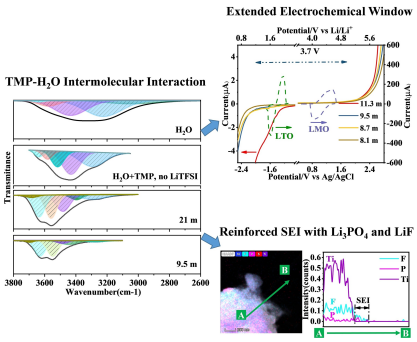

LiTFSI-TMP-H_2O electrolytes with an expanded electrochemical stable window of 3.7 V are rationally designed by controlling intermolecular interaction and interphase chemistry. Benefiting from reduced H_2O activity and reinforced solid electrolyte interphase, the assembled water-tolerance $LiMn_2O_4||Li_4Ti_5O_{12}$ full cell with a limited P/N ratio of 1.14 can achieve a long cycling life with high coulombic efficiency.